Journal of Space Safety Engineering xxx (xxxx) xxx

Contents lists available at ScienceDirect

Journal of Space Safety Engineering

journal homepage: www.elsevier.com/locate/jsse

# Serendipitous detection of orbital debris by the International Liquid Mirror Telescope

Paul Hickson[a,b,*], Bhavya Ailawadhi[c,d], Arun S[c], Monalisa Dubey[c,e], Naveen Dukiya[c,e], Sara Filali[f], Brajesh Kumar[c,g], Kuntal Misra[c], Vibhore Negi[c,d], Kumar Pranshu[c,h], Jean Surdej[f], Saakshi Turakhia[a]

[a] Department of Physics and Astronomy, The University of British Columbia, 6224 Agricultural Road, Vancouver, V6T 1Z1, BC, Canada
[b] Outer Space Institute, The University of British Columbia, 325-6224 Agricultural Road, Vancouver, V6T 1Z1, BC, Canada
[c] Aryabhatta Research Institute of Observational Sciences, Manora Peak, Nainital, 263001, Uttarakhand, India
[d] Deen Dayal Upadhyay Gorakhpur University, Civil Lines, Gorakhpur, 273009, Uttar Pradesh, India
[e] Mahatma Jyotiba Phule Rohilkhand University, Pilibhit Bypass Road, Bareilly, 243006, Uttar Pradesh, India
[f] Institut d'Astrophysique et de Géophysique, Université de Liège, 19 C Allée du 6 août, Liège (Sart-Tilman), B-4000, Belgium
[g] South-Western Institute for Astronomy Research, Yunnan University, Kunming, 650500, Yunnan, PR China
[h] University of Calcutta, 87/1 College Street, Kolkata, 700073, India

ARTICLE INFO

*Article history:*
Received 3 April 2024
Received in revised form 3 May 2024
Accepted 18 May 2024
Available online xxx

*Keywords:*
Orbital debris
Orbital environment
Light pollution

ABSTRACT

The International Liquid Mirror Telescope is a 4-m zenith-pointing optical telescope that employs a rotating liquid primary mirror. Located in the Indian Himalayas, it began operations in October 2022. The telescope is equipped with a CCD camera that has a 22 x 22 arcmin field of view and employs time-delay integration readout to compensate for the Earth's rotation. While its primary purpose is to conduct astronomical survey observations using broad-band filters, the telescope is also sensitive to objects in Earth orbit that pass through its field of view, leaving detectable streaks. We have examined all images obtained during the first year of observations and determined the transit times and position angles of all detected objects. These were compared with publicly available two-line elements, propagated to the time of observation, in order to identify cataloged objects. A total of 301 streaks were found in 1838 images. Of these, 64% were identified with cataloged objects. Most of the identified objects are in low-Earth orbit, in the altitude range of 400–1600 km. The apparent magnitudes of the identified objects range from 3.6 to 15.1 in the V band. It was also possible to infer angular rates, apparent magnitudes and altitudes for 29% of the unidentified objects. The V-band magnitudes range from 6.4 to 19.5 and the estimated altitudes range from 285 to over 300,000 km.



## 1. Introduction

Orbital debris poses an increasing risk to space assets. At present, more than 28,000 resident space objects (RSOs) are tracked by NORAD and appear in the public database available at Space-Track.org. These include satellites, rocket boosters and orbital debris. It is expected that there are many more undetected objects that pose a significant collision risk, particularly to satellites in low-Earth orbit (LEO) [1,2]. The advent of constellations potentially containing tens of thousands of satellites will greatly increase the number of RSOs [3]. The astronomical impact of these objects has long been recognized, but contamination of astronomical images by satellite and debris tracks is now becoming increasingly problematic [4–10].

Two years ago, a new ground-based optical telescope began operation. The International Liquid Mirror Telescope (ILMT) is a 4-m zenith-pointing telescope located at a latitude of 29.36° N on Devasthal Peak in the Indian Himalayas [11]. The telescope is fixed, pointing at the zenith, and is used for astronomical surveys. RSOs passing near the zenith produce streaks in the images acquired by the telescope. This provides a unique opportunity to serendipitously monitor the orbital environment [12]. On average approximately 100 cataloged objects pass through the field of view of the ILMT each day. Typically about 6% of these transit during dark

* Corresponding author
*E-mail address:* hickson@physics.ubc.ca (P. Hickson).

https://doi.org/10.1016/j.jsse.2024.05.003


Please cite this article as: P. Hickson, B. Ailawadhi, A. S et al., Serendipitous detection of orbital debris by the International Liquid Mirror Telescope, Journal of Space Safety Engineering, https://doi.org/10.1016/j.jsse.2024.05.003

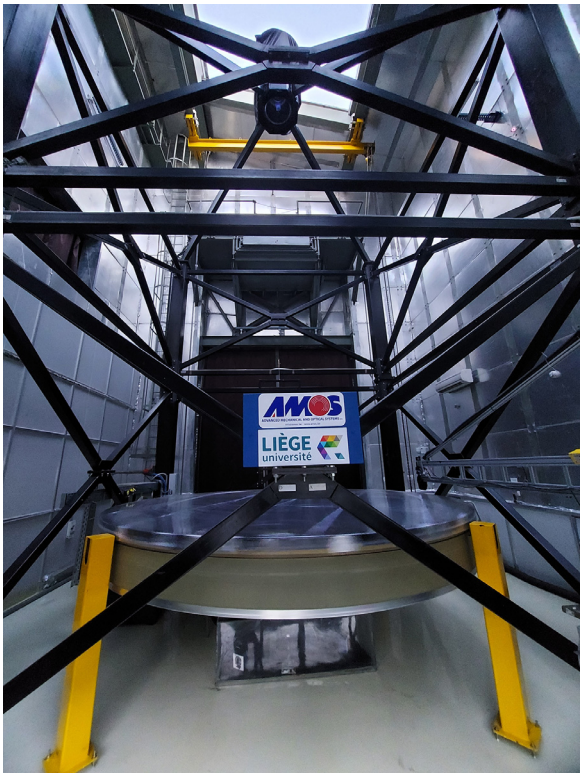


**Fig. 1.** Side view of the ILMT taken with a fish-eye lens. The mirror can be seen in the center, supported by the air bearing. The optical corrector and camera are located in the cylinder at the top of the telescope structure.

hours (when the Sun is more than 18° below the horizon) while also being illuminated by the Sun. These can potentially be detected by the telescope.

The ILMT observing season extends from October until June. No observations are conducted during the summer months due to the monsoon. The telescope began operation in October 2022, with time divided between science observations and engineering. This paper presents an analysis of the 64 nights of science observations obtained during the first observing season. This work extends initial results that were based on the first 10 nights of observations [13].

## 2. Observations and analysis

The ILMT, shown in Fig. 1, utilizes the principle that the equilibrium surface of a liquid rotating at constant speed about a vertical axis in a uniform gravitational field is a paraboloid. The mirror consists of a carbon-fiber parabolic dish supporting a 3 mm film of liquid mercury. It is mounted on an air bearing, which facilitates smooth rotation, and is driven by a brushless DC motor integrated within the air bearing. A control system maintains a constant rotation period of 8.028 s with a variation that is typically less than one part per million. A mylar film of 2.5 $\mu$m thickness is placed above the mercury surface and rotates with the mirror. Its purpose is to protect the liquid from air disturbances that result from wind and mirror rotation.

The telescope is equipped with a refractive prime-focus corrector that provides a 40-arcmin diameter well-corrected field of view. Its novel five-element design compensates for star-trail curvature effects [14], resulting in sharp images with a quality limited primarily by atmospheric turbulence. The detector is a 16-MPixel charge-coupled device (CCD) camera which images a 0.373°× 0.373° region of the sky centred on the zenith. There is no shutter, so the CCD views the sky continuously. In order to compensate for image motion due to the Earth's rotation, the CCD is operated in time-delay integration (TDI) mode, in which it is scanned continuously. As a result, photoelectrons are moved along the CCD columns at the same rate as the star images, and the CCD is read out continuously. In this way sharp images of stars and celestial objects are obtained. Objects that move, with respect to the stars, are trailed, leaving streaks in the images. The intensity in a streak may vary periodically if the object is rotating.

The size of a TDI image is not limited to the size of the CCD. Because the CCD is scanned continuously, the number of pixels in the scan direction (i.e. right ascension) can be arbitrarily large. In practice it is limited by the storage capacity of the computer. For these observations, two image formats were employed. The "small" format is 4096 × 4096 pixels, corresponding to the physical size of the CCD. This format is normally used for engineering, such as focus, alignment and image quality checks. However, most images are "large" format, having 36864 × 4096 pixels (3.348° × 0.373°).

The telescope employs three optical filters, corresponding to the Sloan Digital Sky Survey g', r' and i' wavelength bands [15]. The filter is normally selected at sunset and used throughout the night. Color information can be obtained for astronomical objects, and for RSOs that are observed on more than one night, by selecting a different filter each night.

The ILMT saw first light in April 2022 and began a period of commissioning in October during which both scientific and engineering images were obtained.

The data set used for the present study comprises 1838 images acquired between October 23, 2022 and June 15, 2023, inclusive. The effective integration time for celestial objects was 102.36 s, which is the time interval for their images to cross the CCD. The effective integration time for RSOs is usually much less as they generally move at high angular rates, crossing the detector in just a few seconds, or less.

Each image was pre-processed to remove sensitivity variations and dark current. Spatial variations in the background level were removed by high-pass median filtering. The images were astrometrically and photometrically calibrated using Gaia stars present in the image. After processing, the images were searched visually for linear tracks. Detected tracks were then measured to determine the length, width, orientation, integrated flux and signal-to-noise ratio (SNR).

A complete set of publicly-available two-line elements (TLEs) was downloaded from Space-Track.org, for the period extending from 30 days before to 30 days after the observations. A list of current TLEs was then generated for each night of observation by selecting, for every cataloged object, the TLE whose epoch was closest to the time of observation. The time difference between the epoch of the selected TLE and the time of observation was typically less than two or three days, and in no case was it more than 30 days. This formed our comparison data set. Each TLE in this set was then propagated, using the SGP4/SDP4 algorithm [16,17], and the times and orbital parameters for all objects passing near the zenith were determined. A calculation was performed to determine which objects were illuminated by the Sun at those times. The data analysis and TLE propagation were performed using the OCS software package [18].

A comparison was then made of the catalog lists and the detected streaks. A cataloged object was deemed to be *correlated* (identified) if all of the following conditions were met:

1. The object passed within 0.3 degrees of the zenith.
2. The time of passage was within ± 3 minutes of the time of observation.
3. The position angle of the object was within ± 3° of the measured position angle of the observed streak.

The 3 minute time limit is sufficiently large to accommodate errors in the time recorded by the image acquisition system, uncertainties in the exact position of the CCD, and uncertainties in the TLE. The 3° position angle limit is twenty times the observed standard deviation of 0.16° in the position angle differences. One object had a position angle error of 1.96°, but it had a very short track that resulted in a large position-angle uncertainty.

The integration time for an object is the length of time that the object's image was on the detector. For correlated objects, the angular rate $\omega$ can be computed from the TLE. From the measured track length $s$, the integration time is

$$\Delta t = \frac{s}{\omega}. \tag{1}$$

The apparent magnitude of the object can then be obtained from the measured flux $F$ as

$$m = m_0 - 2.5 \log_{10}\left(\frac{F}{\Delta t}\right), \tag{2}$$

where $m_0$ is the magnitude zero point obtained from the photometric calibration of the image.

The angular rates, and therefore the magnitudes, of uncorrelated objects are generally unknown. However, it is possible to estimate these if both ends of the track are contained within the image. We refer to these as *entire* tracks. They happen if an object crosses the CCD in an easterly or westerly direction, without reaching the north or south edge of the CCD. In fact, for fast-moving objects, the direction of motion can also be determined, as a consequence of the TDI mode of operation. This is possible because the pixel number in the $x$ (right ascension) direction is directly related to the time at which the readout occurred.

This is most easily seen in the Earth-centred inertial (ECI) reference frame. As the Earth rotates, the optical axis of the telescope moves across the sky at an angular rate $\omega_s = 15.041 \cos(l)$ arcsec s$^{-1}$, where $l$ is the latitude of the observatory. Our convention is that angular rates increase in the west-to-east direction (i.e. a prograde orbit). An object moving with east-west angular rate $\omega_x$ will cross the detector in a time

$$\Delta t = \frac{L_x}{|\omega_x - \omega_s|}. \tag{3}$$

where $L_x$ is the angular size of the CCD in the east-west direction. The length of the east-west component of the object's track length will therefore be

$$s_x = |\omega_x \Delta t| = \left|\frac{\omega_x L_x}{\omega_x - \omega_s}\right|. \tag{4}$$

This function is shown in Fig. 2, in the dimensionless form $s_x/L_x$ vs $\omega_x/\omega_s$. We see that fast-moving objects ($|\omega_x| \gg \omega_s$) have track lengths comparable to $L_x$. For those in prograde orbits, the track length is greater than $L_x$ and for those in retrograde orbits it is less than $L_x$. For slow-moving objects ($|\omega_x| \lesssim \omega_s$) it is not possible to distinguish prograde from retrograde motion. For any track length there are two possible values of $\omega_x$. Values in the range $0 < \omega_x < \omega_s/2$ correspond to objects beyond geosynchronous orbit (GEO), which are less likely to be detected. When estimating the angular rate from the track length, we therefore chose the value that corresponds to faster-moving objects, $\omega_x < 0$ and $\omega_x > \omega_s/2$. Thus our estimate of the object's east-west angular rate is

$$\omega_x = \frac{\omega_s}{1 - L_x/s_x}. \tag{5}$$

and the integration time becomes

$$\Delta t = \frac{|s_x - L_x|}{\omega_s}. \tag{6}$$

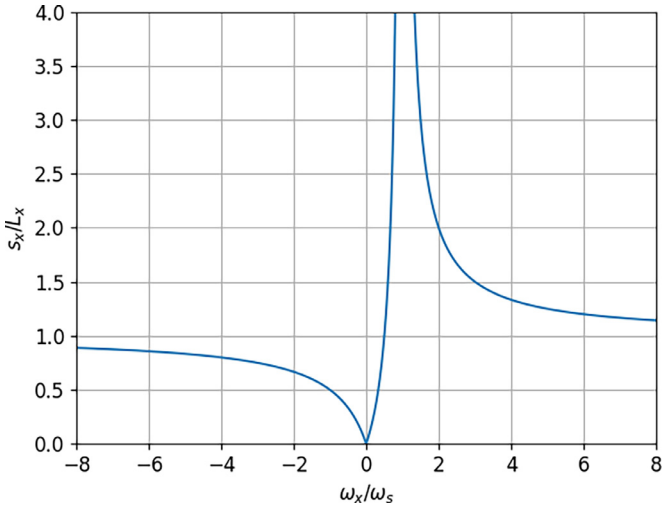


**Fig. 2.** The east-west component, $s_x$, of the track length of an object is shown as a function of the east-west component, $\omega_x$, of the object's angular rate.

**Table 1**
Observations and results.

| Parameter | Value |
|---|---|
| Detector area | 0.139 sq. deg. |
| Pixel size | 0.327×0.327 arcsec |
| Image format (pixels) | 4096×4096, 36864×4096 |
| Number of images | 1838 |
| Total observing time | 307.2 hr |
| Number of streaks found | 301 |
| Number of correlated objects | 192 |
| Satellite fraction | 64.1% |
| Rocket body fraction | 20.3% |
| Debris fraction | 15.6% |
| V magnitude range of correlated objects | 3.6 - 15.1 |
| Median V magnitude of correlated objects | 8.2 |
| Altitude range of correlated objects | 484 - 26,894 km |
| Median altitude of correlated objects | 1,207 km |
| Number of uncorrelated objects | 109 |
| Fraction uncorrelated | 36.2% |
| V magnitude range of uncorrelated objects | 6.4 - 19.5 |
| Median V magnitude of uncorrelated objects | 13.8 |
| Altitude range of uncorrelated objects | 285 - 305,544 km |
| Median altitude of uncorrelated objects | 13,235 km |

The apparent magnitude can now be determined from the measured flux in the track, in the same manner as for correlated objects.

The total angular rate is

$$\omega = \frac{s}{\Delta t}, \tag{7}$$

where $s$ is the total track length. The altitude $a$ of the object can now be determined if a circular orbit is assumed. This is done by solving the cubic equation

$$x^3 + (1 + 2b)x^2 + (c + 2b)x + c - d = 0, \tag{8}$$

where

$$b = \frac{\omega_s \omega_x}{\omega^2}, \tag{9}$$

$$c = \frac{\omega_s^2}{\omega^2}, \tag{10}$$

$$d = \frac{GM}{\omega^2 R^3}. \tag{11}$$

Here $M$ and $R$ are the mass and mean radius of the Earth, and $x = a/R$.

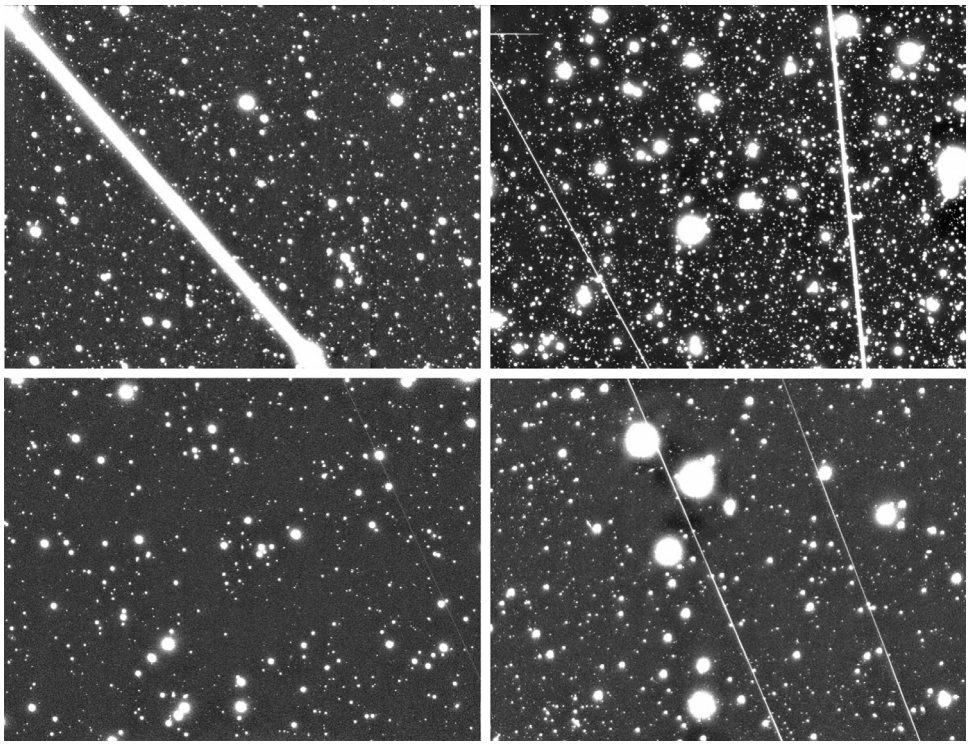

**Fig. 3.** Montage showing streaks produced by six correlated objects detected by the ILMT. Clockwise from top left are STARLINK 1450, FREJA, METEOR 2-15, SL-6 R/B, COSMOS 2063, SL-12 R/B. These have V magnitudes ranging from 3.6 to 15.1. The individual images cover 29 x 22 arcmin.

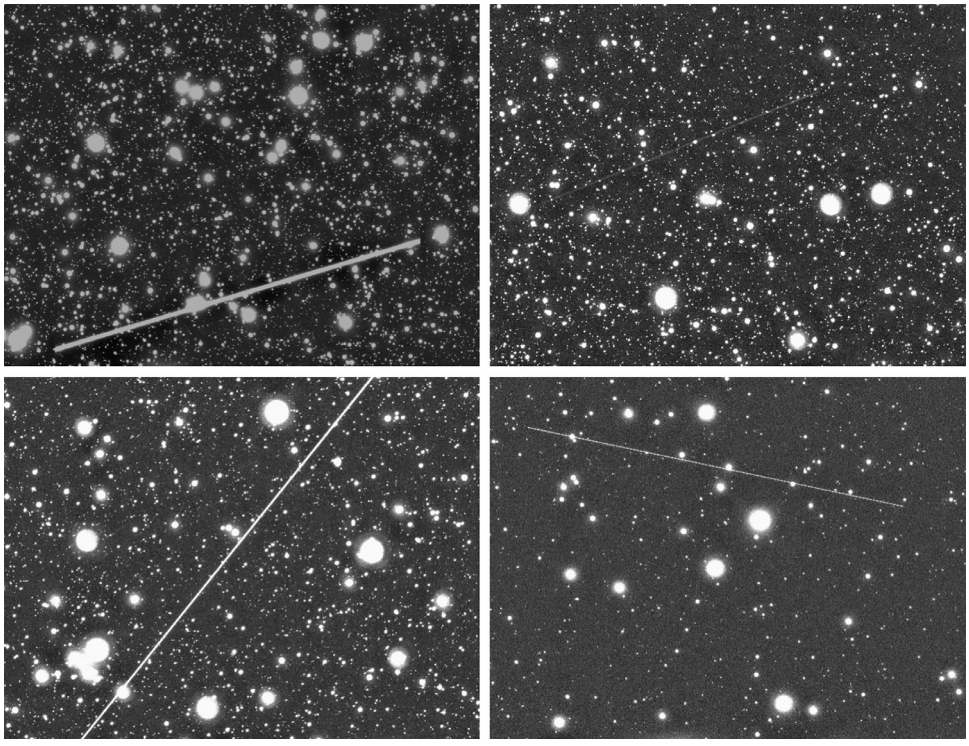

**Fig. 4.** Montage showing streaks produced by four uncorrelated objects detected by the ILMT. The individual images cover 29 x 22 arcmin.

## 3. Results

Our results are summarized in Table 1. A total of 301 streaks were identified in the ILMT images. 64% of these were correlated with cataloged objects. Six examples of tracks produced by correlated objects are shown in Fig. 3 and four examples of tracks produced by uncorrelated objects are shown in Fig. 4.

### 3.1. Properties of correlated objects

Apparent magnitudes derived from the flux in the track were transformed to the V (visual) band assuming a solar spectrum, using color indices for a star of spectral type K2V and Gaia DR3 photometric transformations [19,20]. The V magnitude distribution is shown in Fig. 5. The magnitudes range from 3.6 to 15.1 with a me-

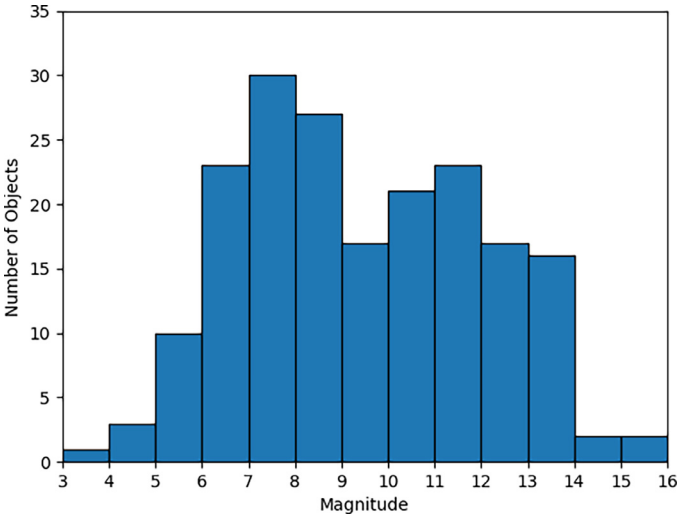


**Fig. 5.** Apparent V magnitude distribution of correlated RSOs.

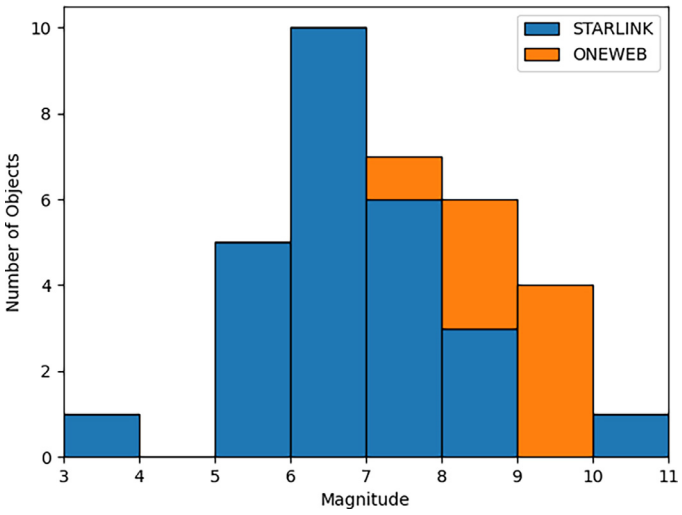


**Fig. 7.** Apparent V magnitude distribution of observed Starlink and OneWeb satellites.

dian of 8.2. The faintest correlated object is a rocket body with an apparent V magnitude of 15.1, detected with a SNR of 110.

The altitude distribution for the correlated objects is shown in Fig. 6. We find that 61% have altitudes below 2000 km. There is a significant bias towards high-altitude objects as these are more likely to be illuminated by the Sun, due to the geometry of the Earth's shadow at the latitude of the ILMT. Because of this, the LEO objects can only be seen within a few hours of sunrise or sunset. The distribution of these objects has a significant peak in the 400–600 km altitude range, and a sharp drop above 1600 km. Higher altitude objects are found to nearly 27,000 km, with a mild concentration around 20,000 km. We did not see any objects in geosynchronous orbit, but that is to be expected due to the latitude of the observatory.

### 3.2. Properties of uncorrelated objects

A total of 32 uncorrelated objects (29%) have entire tracks. For these, angular rates, altitudes and apparent V magnitudes, were estimated. The magnitude distribution of these objects is shown in Fig. 8. The magnitudes range from 6.4 to 19.5, with a median value of 13.8. The altitude distribution is shown in Fig. 9. The altitudes ranged from 285 to 305,544 km. Seven uncorrelated objects, have altitudes greater than 40,000 km, and are not shown in the figure. One object had a very high angular rate ($3^\circ$ $s^{-1}$). It is likely to be a meteor, and was excluded from further consideration. Of the 14 uncorrelated objects having altitudes below 7000 km, 6 have prograde orbits and 8 have retrograde orbits.

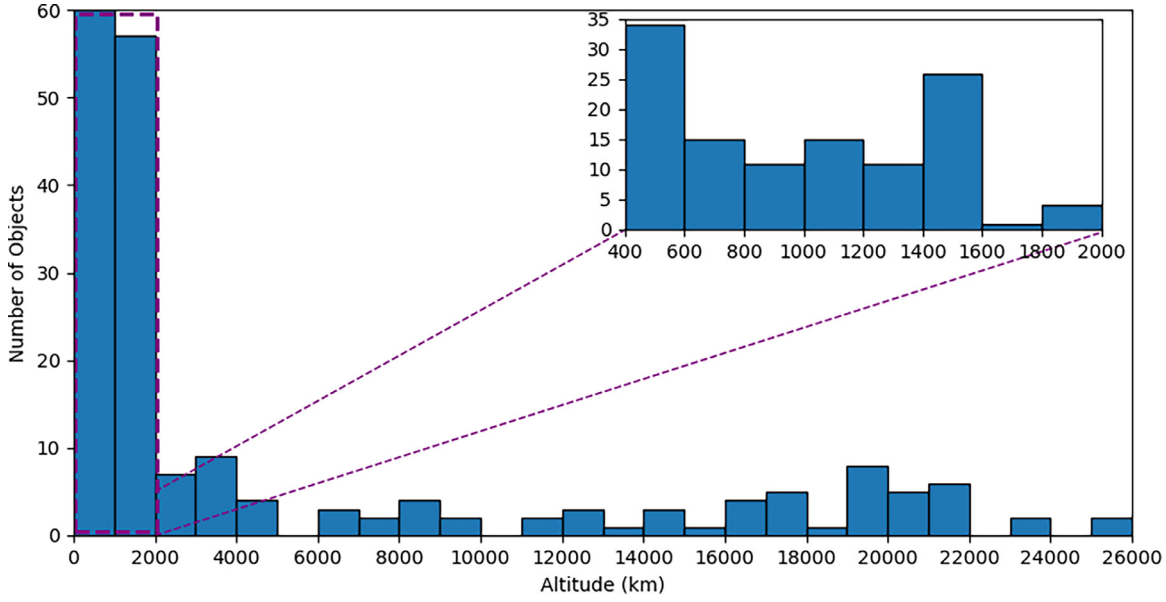


**Fig. 6.** Altitude distribution of correlated RSOs.

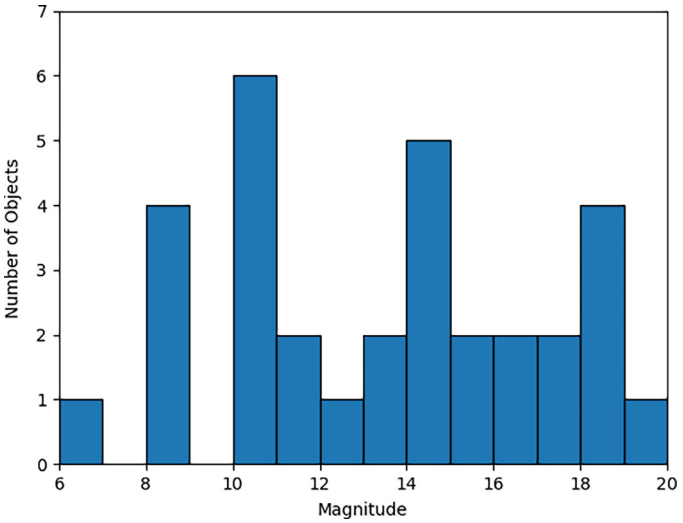


**Fig. 8.** Apparent V magnitude distribution of uncorrelated objects.

## 4. Discussion and conclusions

On average, 7.1 detectable objects per square degree per hour pass near the zenith at the latitude of the ILMT. Objects having orbital inclination less than the observatory latitude never reach the zenith and are thus not counted. This is compensated by the fact that at higher latitudes, objects passing overhead are illuminated by the Sun at lower altitudes, due to the geometry of the Earth's shadow, and are thus more likely to be seen.

Roughly two-thirds of the detected objects were identified by correlation with available orbital-element data. The remaining, uncorrelated, objects are unidentified. They have a median V magnitude that is 5.6 magnitudes fainter than that of the correlated objects. Roughly two-thirds of the correlated objects have estimated altitudes below 2000 km, compared to one-third for the uncorrelated objects. Of the uncorrelated objects that have estimated altitudes below 7000 km, for which the direction of motion can be reliably estimated, there are an equal number of prograde and retrograde orbits, within the statistical error. Seven objects have an estimated altitude greater than 40,000 km. All are uncorrelated. The most distant of these has an angular rate of just 1 arcsec $s^{-1}$. If it is in Earth orbit, that corresponds to an orbital radius that is 80% of that of the Moon. If it has an albedo comparable to that of the Moon, its diameter would be approximately 2 m. Alternatively, if it is orbiting the Sun, with a velocity comparable to that of the Earth, it would be more than an order of magnitude further away and have a diameter on the order of 40 m.

Streaks from bright objects are a concerning source of contamination for astronomical observations. Many of the streaks that we detected are as wide as 12 arcsec and far brighter than the faint stars and galaxies that they cross. Subtraction of the streaks is problematic due to the high levels of photon noise that they produce, and intrinsic variations in brightness as the objects rotate [21].

Of particular concern are satellites launched by non-governmental entities such as Starlink and OneWeb, due to the very large numbers that are planned. Fig. 7 shows the observed apparent magnitude distribution of Starlink and OneWeb satellites. The mean apparent magnitudes are 6.7 and 8.6 respectively. The difference is largely due to the higher altitudes of the OneWeb satellites (the mean altitudes are 546 km and 1203 km for Starlink and OneWeb respectively). More than half of the Starlink satellites that we observed are brighter than the International Astronomical Union recommended minimum magnitude of 7 [22].

As satellite mega-constellations continue to expand, it becomes increasingly important to develop measures to mitigate their astronomical impact [23]. It will be necessary to find effective ways to reduce both the amount of sunlight that their satellites reflect and the infrared radiation that they emit. Astronomical observations will be essential to assess the success of these measures [24].

These results demonstrate the potential of the ILMT for the serendipitous detection of satellites and orbital debris. More than a third of the objects that we detected could not be matched to cataloged objects. Some may be meteors, but most are likely to be classified military satellites and previously-undetected orbital de-

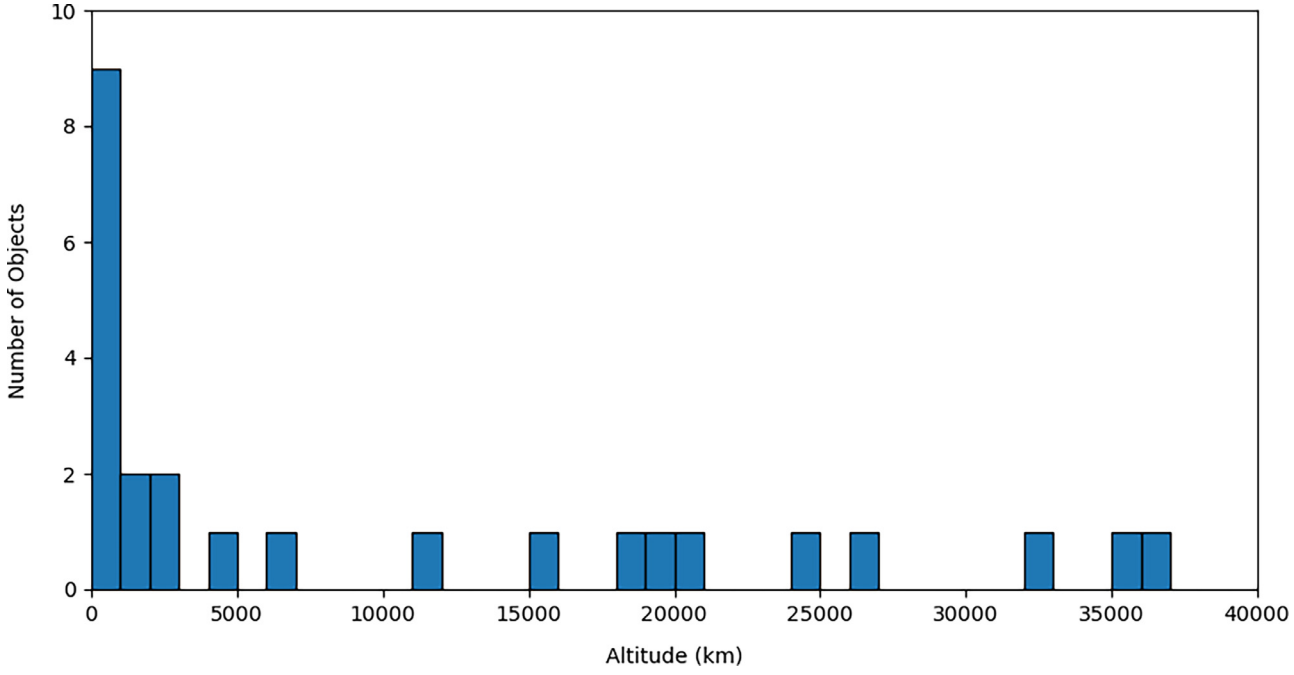


**Fig. 9.** Altitude distribution of uncorrelated objects. Seven objects have altitudes above 40,000 km and are not shown.

bris. This would indicate a significant level of incompleteness, or inaccuracy, of TLEs in the public database.

In full-time operation, the ILMT is expected to obtain on the order of 1500 clear dark hours of observations per year, which is roughly five times the present data set. This will provide a unique opportunity to monitor the increasingly-crowded space environment.

## Declaration of competing interest

The authors declare that they have no known competing financial interests or personal relationships that could have appeared to influence the work reported in this paper.

## CRediT authorship contribution statement

**Paul Hickson:** Conceptualization, Data curation, Methodology, Formal analysis, Funding acquisition, Investigation, Validation, Visualization, Software, Writing – original draft, Writing – review & editing. **Bhavya Ailawadhi:** Investigation. **Arun S:** Investigation. **Monalisa Dubey:** Investigation. **Naveen Dukiya:** Investigation. **Sara Filali:** Investigation. **Brajesh Kumar:** Investigation. **Kuntal Misra:** Project administration, Resources, Supervision. **Vibhore Negi:** Investigation. **Kumar Pranshu:** Investigation. **Jean Surdej:** Conceptualization, Funding acquisition, Investigation, Project administration, Resources, Supervision, Writing – review & editing. **Saakshi Turakhia:** Investigation, Visualization, Writing – review & editing.

## Acknowledgments

The 4-m International Liquid Mirror Telescope (ILMT) project results from a collaboration between the Institute of Astrophysics and Geophysics (University of Liège, Belgium), the Universities of British Columbia, Laval, Montreal, Toronto, Victoria and York University, and the Aryabhatta Research Institute of Observational Sciences (ARIES, India). The authors thank Hitesh Kumar, Himanshu Rawat, Khushal Singh and other observing staff for their assistance. The team acknowledges the contributions of ARIES's past and present scientific, engineering and administrative members in the realization of the ILMT project. We thank the referee for calling attention to the possibility of estimating angular rates for uncorrelated objects that have entire tracks, and Aaron Boley for calling attention to the impact of latitude on satellite visibility. PH acknowledges financial support from the Natural Sciences and Engineering Research Council of Canada, RGPIN-2019-04369. JS wishes to thank Service Public Wallonie, F.R.S.–FNRS (Belgium) and the University of Liège, Belgium for funding the construction of the ILMT. PH and JS thank ARIES for hospitality during their visits to Devasthal. BA acknowledges the Council of Scientific & Industrial Research (CSIR) fellowship award (09/948(0005)/2020-EMR-I) for this work. MD acknowledges Innovation in Science Pursuit for Inspired Research (INSPIRE) fellowship award (DST/INSPIRE Fellowship/2020/IF200251) for this work. This work has made use of data from the European Space Agency (ESA) mission Gaia (https://www.cosmos.esa.int/gaia), processed by the Gaia Data Processing and Analysis Consortium (DPAC, https://www.cosmos.esa.int/web/gaia/dpac/consortium). Funding for the DPAC has been provided by national institutions, in particular the institutions participating in the Gaia Multilateral Agreement.

## References

[1] D.J. Kessler, B.G. Cour-Palais, Collision frequency of artificial satellites: the creation of a debris belt, J. Geophys. Res.: Space Phys. 83 (A6) (1978) 2637–2646, doi:10.1029/JA083iA06p02637.
[2] J.-C. Liou, N.L. Johnson, Risks in space from orbiting debris, Science 311 (2006) 340–341.
[3] R. Massey, S. Lucatello, P. Benvenuti, The challenge of satellite megaconstellations, Nature Astron. 4 (2020) 1022–1023.
[4] A.C. Boley, M. Byers, Satellite mega-constellations create risks in low earth orbit, the atmosphere and on earth, Sci. Rep. 11 (2021) 10642.
[5] S.M. Lawler, A.C. Boley, H. Rein, Visibility predictions for near-future satellite megaconstellations: latitudes near 50° will experience the worst light pollution, Astronomic. J. 163 (1) (2021) 21, doi:10.3847/1538-3881/ac341b.
[6] M.M. Shara, M.D. Johnston, Artificial earth satellites crossing the fields of view of, and colliding with, orbiting space telescopes, Publ. Astronomic. Soc. Pacific 98 (606) (1986) 814–820.
[7] O.R. Hainaut, A.P. Williams, Impact of satellite constellations on astronomical observations with ESO telescopes in the visible and infrared domains, Astron. Astrophys. 636 (2020) A121, doi:10.1051/0004-6361/202037501.
[8] A. Venkatesan, J. Lowenthal, P. Prem, M. Vidaurri, The impact of satellite constellations on space as an ancestral global commons, Nature 4 (2020) 1043–1048.
[9] S. Kruk, P. Garcia-Martin, M. Popescu, B. Aussel, S. Dillmann, M. Perks, T. Lund, B. Merin, J.R. Thomson, S. Karadag, M. McCaughrean, The impact of satellite trails on hubble space telescope observations, Nature Astron. 7 (2023) 1–7, doi:10.1038/s41550-023-01903-3.
[10] S. Nandakumar, S. Eggl, J. Tregloan-Reed, C. Adam, J. Anderson-Baldwin, M.T. Bannister, A. Battle, Z. Benkhaldoun, T. Campbell, J.P. Colque, G. Damke, I. Plauchu Frayn, M. Ghachoui, P.F. Guillen, A. Ettahar Kaeouach, H.R. Krantz, M. Langbroek, N. Rattenbury, V. Reddy, R. Ridden-Harper, B. Young, E. Unda-Sanzana, A.M. Watson, C.E. Walker, J.C. Barentine, P. Benvenuti, F. Di Vruno, M.W. Peel, M.L. Rawls, C. Bassa, C. Flores-Quintana, P. Garclá, S. Kim, P. Longa-Peña, E. Ortiz, A. Otarola, M. Romero-Colmenares, P. Sanhueza, S. G, M. Soto, The high optical brightness of the BlueWalker 3 satellite, Nature (2023), doi:10.1038/s41586-023-06672-7.
[11] J. Surdej, P. Hickson, E. Borra, J.-P. Swings, S. Habraken, T. Akhunov, P. Bartczak, H. Chand, M. De Becker, L. Delchambre, F. Finet, B. Kumar, A. Pandey, A. Pospieszalska, B. Pradhan, R. Sagar, O. Wertz, P. De Cat, S. Denis, J. de Ville, M.K. Jaiswar, P. Lampens, N. Nanjappa, J.-M. Tortolani, The 4-m international liquid mirror telescope, Bull. de la Société R. des Sci. de Liège 87 (2018) 68–79.
[12] B. Pradhan, P. Hickson, J. Surdej, Serendipitous detection and size estimation of space debris using a survey zenith-pointing telescope, Acta Astronautica 164 (2019) 77–83, doi:10.1016/j.actaastro.2019.07.008.
[13] P. Hickson, B. Ailawadhi, T. Akhunov, E. Borra, M. Dubey, N. Dukiya, J. Fu, B. Grewal, B. Kumar, K. Misra, V. Negi, K. Pranshu, E. Sun, J. Surdej, Serendipitous detection of orbital debris by the international liquid mirror telescope: first results, Bull. de la Société R. des Sciences de Liège in press (2023).
[14] P. Hickson, E.H. Richardson, A curvature-compensated corrector for drift-scan observations, Publ. Astronomic. Soc. Pacific 110 (1998) 1081–1086.
[15] J.E. Gunn, M. Carr, C. Rockosi, M. Sekiguchi, K. Berry, B. Elms, E. De Haas, u. Ivezić, G. Knapp, R. Lupton, G. Pauls, R. Simcoe, F. Harris, J. Annis, L. Bartozek, W. Boroski, J. Bakken, M. Haldeman, S. Kent, S. Holm, D. Holmgren, D. Petravick, A. Prosapio, R. Rechenmacher, M. Doi, M. Fukugita, K. Shimasakus, N. Okada, C. Hull, W. Siegmund, E. Mannery, M. Blouke, D. Heidtman, D. Schneider, R. Lucino, J. Brinkman, The sloan digital sky survey photometric camera, Astronomic. J. 116 (1998) 3040–3081, doi:10.1038/s41550-023-01903-3.
[16] F.R. Hoots, R.L. Roehrich, Spacetrack Report No. 3: models for propagation of NORAD element sets, Technical Report, Aerospace Defense Center, Peterson Air Force Base, 1980.
[17] D.A. Vallado, P. Crawford, R. Hujsak, T.S. Kelso, Revisiting spacetrack report 3, in: AIAA Astrodynamics Specialists Conference and Exhibit, 2006, pp. 1–88, doi:10.2514/6.2006-6753.
[18] P. Hickson, OCS: a flexible observatory control system for robotic telescopes with application to detection and characterization of orbital debris, in: First International Orbital Debris Conference, in: LPI Contributions, volume 2109, 2019, p. 6066.
[19] E.E. Mamajek, A modern mean dwarf stellar color and effective temperature sequence, http://www.pas.rochester.edu/~emamajek/EEM_dwarf_UBVIJHK_colors_Teff.txt(2022).
[20] J.M. Carrasco, B. Michele, Gaia early data release documentation 5.5.1 (2022). https://gea.esac.esa.int/archive/documentation/GEDR3/Data_processing
[21] J.A. Tyson, Željko Ivezić, A. Bradshaw, M.L. Rawls, B. Xin, P. Yoachim, J. Parejko, J. Greene, M. Sholl, T.M.C. Abbott, D. Polin, Mitigation of LEO satellite brightness and trail effects on the Rubin Observatory LSST, Astronomic. J. 160 (5) (2020) 226, doi:10.3847/1538-3881/abba3e.
[22] IAU Committee on the Peaceful Uses of Outer Space, Recommendations to keep dark and quiet skies for science and society, https://www.iau.org/static/publications/uncopuos-stsc-crp-8jan2021.pdf(2021).
[23] A. Williams, O. Hainaut, A. Otarola, G.H. Tan, G. Rotola, Analysing the impact of satellite constellations and ESO's role in supporting the astronomy community, The Messenger 184 (2021) 3–7.
[24] J. Tregloan-Reed, A. Otarola, E. Unda-Sanzana, B. Haeussler, F. Gaete, J.P. Colque, C. González-Fernández, J. Anais, V. Molina, R. González, E. Ortiz, S. Mieske, S. Brillant, J.P. Anderson, Optical-to-NIR magnitude measurements of the starlink LEO darksat satellite and effectiveness of the darkening treatment, Astron. Astrophyics 647 (2021).